Korean J. Chem. Eng., 33(7), 2018-2026 (2016)
DOI: 10.1007/s11814-016-0001-1

pISSN: 0256-1115
eISSN: 1975-7220

Highly efficient Al-doped ZnO : Ag catalyst for RB19 photocatalytic degradation: Microwave-assisted synthesis and characterization

Mohamad Reza Khodadadi*, Mohamad Ebrahim Olya,†, and Alireza Naeimi*****

*Department of Nanotechnology, Semnan University, Semnan, Iran
**Department of Environmental Research, Institute for Color Science and Technology, P. O. Box 16765-654, Tehran, Iran
***Department of Nanomaterial's and Nanocoatings, Institute for Color Science and Technology, P. O. Box 16765-654, Tehran, Iran

(*Received 24 December 2014 • accepted 1 January 2016*)

Abstract−ZnO : Ag·Al nano-catalyst was synthesized by microwave technique. The characterization and evaluation of this semiconductor catalyst was examined in contrast with ZnO and ZnO : Ag by X-ray diffraction (XRD), scanning electron microscopy (SEM), tunneling electron microscopy (TEM) and Fourier transform infrared (FTIR) spectroscopy. Thermodynamic study of combustion synthesis showed the reaction temperature for ZnO : Ag·Al samples decreased to 481.48 °C compared to ZnO that is 1141 °C. Tauc's plot was used to calculate the band gap of samples and the location of absorption edge was found at 380 nm. Different molar ratios of Ag and Al were examined to find the best activity of catalyst. In this study, reactive blue 19 (RB19) as a water pollution was used to find the efficiency of catalyst, and the effect of pH on the reaction was studied in a batch reactor under UV radiation. Also, the recyclability experiments confirm that the synthesized ZnO : Ag·Al (7 mole% Ag and 3% mole Al) has responsible photocatalytic activity as compared to ZnO at a similar operating condition.

Keywords: Nano-catalyst, Doping, Band Gap, Recyclability, Reactive Blue 19

INTRODUCTION

Nano semiconductor materials, especially zinc oxide as a prominent metal oxide with its exceptional properties, have attracted experts' attention. This semiconductor is known for high chemical stability, low toxicity, photocatalytic responsibility, low cost, high efficiency, environmentally friendly, excellent optical and piezoelectric [1,2]. It's an important N-type semiconductor with wurtzite structure, a wide-band gap of (2.92 eV-3.37 eV) and high excitation binding energy (60 meV) [3-5]. Innovative developments of using zinc oxide include a variety of applications and devices like optics, gas sensors, diodes, catalysts, solar cells and widely employed in the textile, paint, ceramic and glass industries [6]. Among ZnO properties, poor photon absorption limitation decreases its achievement of high optical features. So, it highly depends on doping with other materials and synthesis methods to reach propitious structures [7,8]. Metal doping is an efficient way to modify the band gap of zinc oxide. There are papers discuss doped materials with ZnO such as: Mg [9], Cd [10], Sn [11] and it was also reported some impurity such as Al and Ag improved photo catalytic activities and enhanced oxygen vacancies [12].

ZnO materials were synthesized through a variety of techniques, such as sol-gel technique [13], pulsed laser deposition [14], plasma-assisted approach [15], thermal CVD [16] and hydrothermal process [17] for different particular applications. All of these methods attempted to incorporate impurity in ZnO and improve lattice point of crystal structures. The main advantage of these techniques is making nanosize ZnO particles; however, unfavorable high synthesis temperature and high degree of technique complexity make them into a challenge. Although, the mentioned methods need expensive instruments, high power pumping system to handle trucculent reaction products, large amount of solution and long time for processing.

Microwave-assisted synthesis is a novel method for producing materials, since microwave heating is an in situ mode of energy conversion, and the microwave heating process is fundamentally different from conventional heating processes. Heat will be generated internally within the material, instead of originating from external sources [18,19]. Microwave processing is low cost due to saving energy, good for synthesis of new materials with unique properties or structures, and it is proper to improve the consistency and efficiency of the products. In addition, minimum energy is required and necessary equipment for combustion synthesis is simple.

The present investigation discusses the efficiency of Al-doped ZnO : Ag catalyst due chemical degradation of Reactive Blue 19 (RB19) as a represent toxic dye in industrial waste water. This dye is widely used in wool textile dyeing, food and cosmetics. To the extent of our knowledge, there are few papers that talk about synthesis of Al doped ZnO : Ag composites regarding degradation of RB19.

MATERIAL AND METHODS

1. Materials

Zinc nitrate hexahydrate ($Zn(NO_3)_2{\cdot}6H_2O$), Silver nitrate ($AgNO_3$),

†To whom correspondence should be addressed.
E-mail: olya-me@icrc.ac.ir

Aluminum nitrate ($Al(NO_3)_3$), glycine and glucose as the ingredients of the final products and Hydrogen peroxide (H_2O_2), H_2SO_4 and NaOH solutions are provided from Merck chemicals. The dye (Reactive Blue 19; C.I. 61200) which has been used for photocatalytic testing of ZnO : Ag·Al is purchased from Alvan Sabet chemical company (Tehran, Iran).

2. Preparation of Al loaded ZnO : Ag

Microwave-assisted hydrothermal process was used to synthesize ZnO : Ag·Al. Zinc nitrate hexahydrate, Zn $(NO_3)_2{\cdot}6H_2O$ (Merck, 99.5%) with known amount of Silver nitrate ($AgNO_3$) (Merck, 99.8%) and Aluminum nitrate $Al(NO_3){\cdot}9H_2O$ (Merck, 99%) as the precursors were used for the synthesis of this nanocomposite. About 5 g $Zn(NO_3)_2{\cdot}6H_2O$ and 0.2 g $AgNO_3$ were dissolved completely into deionized water at 25 °C. Stoichiometric amounts of glucose and glycine were added as fuel solution. To this, different amount of $Al(NO_3){\cdot}9H_2O$ was added and stirred slowly to prepare a level mixture. The mixer was heated at 80 °C to avoid components reaction until a viscous pale yellow gel appeared. A beaker containing the yellow gel was placed into a microwave oven (900 W, 2450 MHz, LG) and after about 60 s of continuous irradiation, the solution started to burn spontaneously such that a foamy porous powder was obtained. Synthesized catalysts contain 7 mol% of Ag (related to ZnO) and set with 3, 7, 15 and 30 mol% of Al (related to ZnO), respectively. The bare ZnO, ZnO : Ag and ZnO : Al were synthesized by the particular procedure, too.

3. Analytical Methods

The composition of synthesized modified ZnO powder was characterized by Fourier-transform infrared (FTIR) spectroscopy using a Perkin-Elmer spectrometer. X-Ray diffraction (XRD) patterns were performed on Cu-Kα (λ=1.54056 A°) radiation in diffraction angle (2θ) range of 10° to 100° with a typical step size of 0.026° with equipment STOE Stadi P to identify crystalline phase. The surface morphology was observed with scanning electron microscopy technique (SEM) using the LEO 1455vp apparatus and TEM using Philips EM 208. Decolorization and photocatalytic activity of treated catalyst was investigated by ultraviolet-visible (UV-vis) absorption double beam spectrophotometer (Perkin-Elmer lambda 25 Model) over the wavelength range of 200 nm to 800 nm.

RESULT AND DISCUSSION

1. Characterization

Characterization of synthesized nano-photocatalysis is presented by XRD, FTIR, SEM and TEM in the following sections.

2. Structural Investigation

X-ray diffraction patterns of combustion synthesized samples are illustrated in Fig. 1. All peaks belong to ZnO structure (JCPDS No. 01-079-2205). The addition of silver nitrate in the combustion precursors leads to formation of metallic silver as a minor phase (JCPDS No. 01-087-0720). Moreover, third structure of $ZnAl_2O_4$ (01-074-1138) is added by co-doping of Ag^+ and Al^{3+} in ZnO structure. This multiphase system depends on the Al^{3+} concentration (above 1% mol) and the rest were expected to form gahnite ($ZnAl_2O_4$) phase. Because of the low solubility of Ag in Zn sites of ZnO structure, shift of ZnO peaks to the lower 2θ and decrease of crystallite size (determined by Scherrer equation) from 51.5 to 43.6 nm are

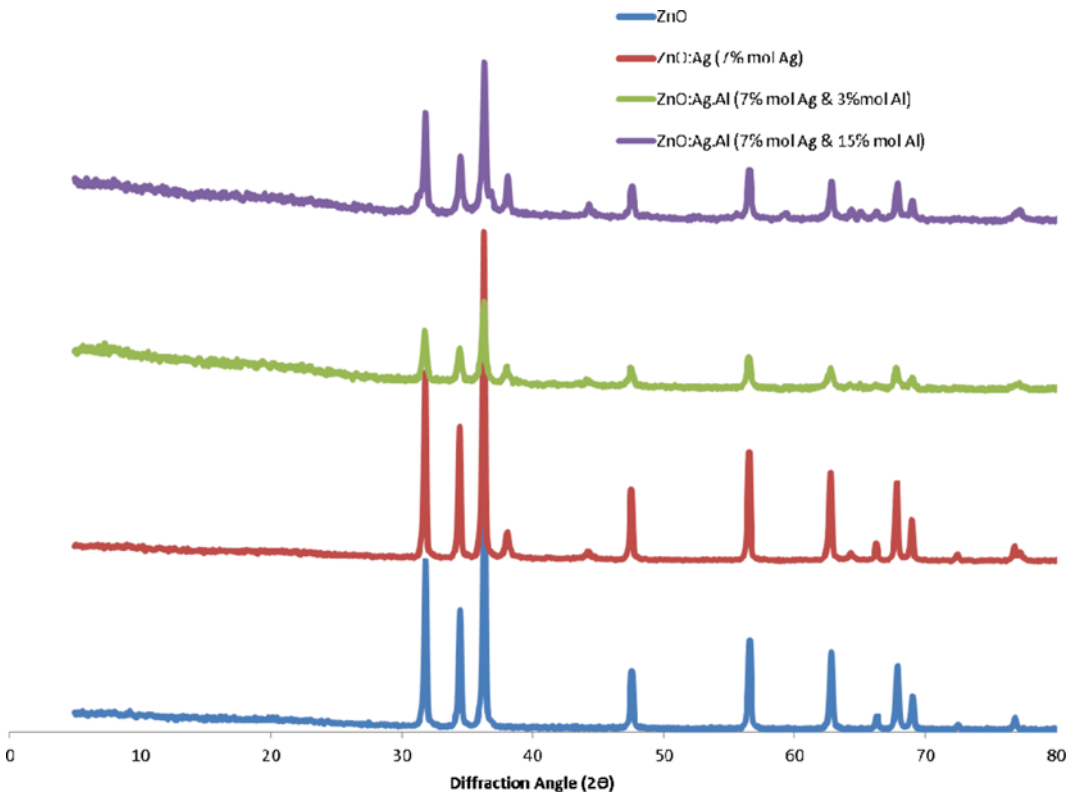

Fig. 1. The XRD patterns of the pure ZnO, ZnO : Ag, Ag-Al co-doped ZnO photocatalysts.

expected. Although, the presence of Ag^{+} has a vital effect on the crystallite size, the addition of Al^{3+} ions beside the Ag^{+} leads to formation of smaller size (42.4 nm). The main reason for low solubility of silver in ZnO structure is due to the large difference of silver (1.26 A°) and zinc (0.74 A°) ion radiuses [1,5,20].

Moreover, the increase or decrease of c/a ratio confirms the thermodynamic changes of combustion reaction. c/a ratio and the distance of crystal plane of hexagonal structures are determined by the following equations:

$$c = \lambda / \mathrm{Sin}\theta \tag{1}$$

$$a = \frac{\lambda}{\sqrt[3]{3}\mathrm{Sin}\theta} \tag{2}$$

$$\frac{1}{d^2} = \frac{4(h^2 + hk^2 + k^2)}{3\ a^2} + \frac{l}{c^2} \tag{3}$$

In these equations, a and c are crystalline lattice constants, d is the plane distance, λ is the wavelength of incident beam of X-ray and θ is the X-ray diffraction angle. The c/a and d_{100} values of ZnO and ZnO : Ag show the same values (c/a=1.44 and d_{100}=2.55 nm). It seems that the presence of Ag ions cannot change the c/a and d values essentially, but crystal size has decreased [21,22]. According to the past studies, the maximum dissolution of Al^{3+} ions in host lattice structure is approximately 1% molar, which the orientation of ions in the vacant lattice space of ZnO leads to an increase in crystalline lattice size [2]. But increasing of Al^{3+} concentration changes the c/a and d_{100} to 1.31 and 2.48 nm. Moreover, interstitial diffusion of Al^{3+} in the ZnO structure can be determined by calculation of bond length in ZnO : Ag and ZnO : Ag·Al structure. These equations determine L value as the bond length in Zn-O lattice [2,21,22]:

$$L = \sqrt{\frac{a^2}{3} + \left(\frac{1}{2} - U\right)^2 \times c^2} \tag{4}$$

$$U = \left(\frac{a^2}{3c^2}\right) + 0.25 \tag{5}$$

The results confirm that the presence of Al^{3+} decreases the Zn-O bond length from 2.033 to 1.99 nm. This fact explains the reason for the lowest crystallite size of ZnO : Ag·Al sample.

Large number of vacancies of oxygen, vacancy clusters, and local lattice disorders are present in the interface of ZnO nanoparticles and doped atoms; there is a decrease in "Zn-O" bonding length and the volume of the unit cell, but there is no apparent change in the positions and intensities of XRD peaks. Average crystallite size decreased when the micro strain increased. This might be due to the mechanical surface-free energy of the metastable nanoparticles [23,24].

From a thermodynamic view, the reduction of crystallite size can be assigned to attempting the system to lowering the change of Gibbs energy (ΔG). The entrance of Ag^{+} instead of Zn^{2+} leads to increase of disordering in the ZnO structure followed by enhancement of entropy. By increasing the positive trend of the change of

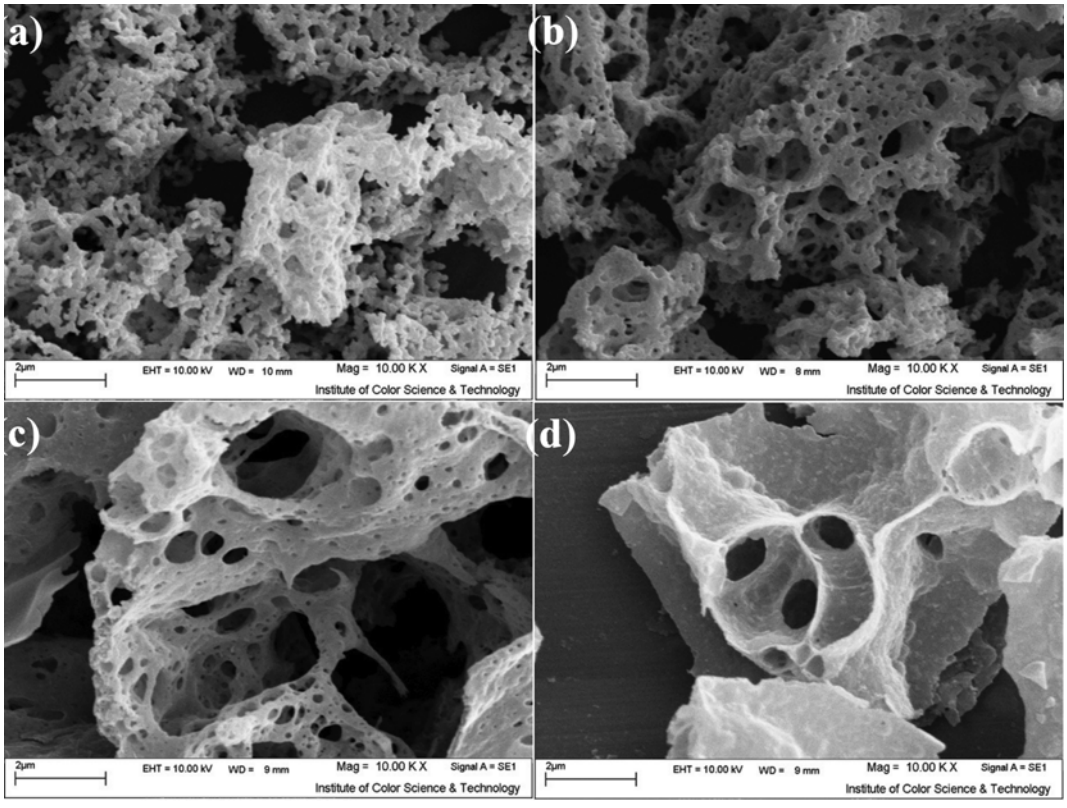

Fig. 2. SEM images of ZnO (a), Ag (7% mol) modified ZnO (b), Ag-Al (7% mol Ag and 3% mol Al) co-doped ZnO (c) and Ag-Al (7% mol Ag and 15% mol Al) co-doped ZnO.

entropy (ΔS), the ΔG shows the negative path corresponds to the Gibbs free energy law (ΔG=ΔH−TΔS). However, the final state of this system depends on the enthalpy of combustion reaction (ΔH) of final product, intensely. This parameter can be affected by flame temperature (T_{ad}). The higher amount of T_{ad} causes the formation of higher temperature, which leads to the higher ΔH value. Kinetic view of these events is the increase of crystal growth rate.

3. Structural Investigation

Fig. 2 shows the morphology of synthesized samples with different silver and aluminum dopant content. Images (Fig. 2(a)) illustrate the agglomerated ZnO clusters that along with have created hollow foam. This foam has porosities with different sizes that are attributed to the combustion synthesis and gasses released in combustion reaction such as (CO_2, NO_2, N_2) [25]. By adding silver nitrate to the prior sample, due to decrease in fuel to oxidant source ratio, combustion intensity rises; therefore, more gas is released and zinc oxide foam has more porosity (Fig. 2(b)) [26]. By increasing aluminum nitrate content in the samples and by formation of $ZnAl_2O_4$ compound, separated and smaller particles are observed, so that this fact causes a variation from hexagonal structure in zinc oxide to spinel structure in $ZnAl_2O_4$ (Fig. 2(c)). With the increasing amount of aluminum nitrate and formation of $ZnAl_2O_4$, it is believed that the combustion deployed has been focused on the wall of plates that the particles have dense plate-like shapes (Fig. 2(d)). The reason for plate formation is due to the combustion characteristic in aluminate structure and the reduction of combustion intensity by adsorbing microwave arrays. These plate diameters which are formed with smaller nanometer particles are reaching to 100 to 200 nm. TEM images of ZnO : Ag·Al sample show particles in 40 to 50 nm sizes that possess regular crystalline structure. Non-regular structures in this sample are dependent on the combustion synthesis conditions and reduction in the ratio of fuel to oxidants (Fig. 3).

4. Thermodynamics of Combustion Synthesis

Thermodynamic studies of the combustion system give us useful information. The reaction enthalpy, ΔH_{298}, is an important parameter that specifies the independency of the chemical reaction. In this synthesis, due to the modification of combustion intensity, two kinds of fuels such as glucose and glycine with 75% and 25% ratios, respectively, are used. In this case, it can be supposed that the ignition of glucose and glycine by microwave arrays provides the necessary energy to the synthesis of the samples. Therefore, ignition of two fuels in the mentioned ratios causes the following reactions and the synthesis of the ZnO samples with silver and aluminum dopants, and the total enthalpy of glucose and glycine ignition is equal to the total combustion system enthalpy. Reaction heat in adiabatic conditions is consumed to raise the combustion products' temperature; therefore, the adiabatic temperature is calculated by the following equation [27,28]:

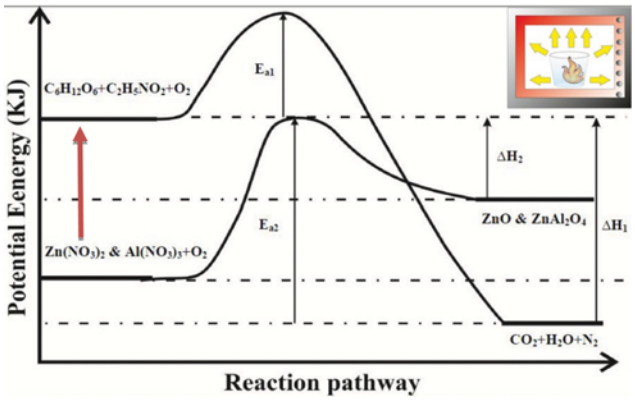

Fig. 4. A view of a combustion reaction.

$$\Delta H^{r}_{T^0}=\int_{T^0}^{T_{ad}} C_p dT \quad (6)$$

where $\Delta H^{r}_{T^0}$ is the reaction enthalpy in T_{ad} and C_p is the heat capacity variations of the reaction products [29]. In this case the combustion flame temperature in the synthesis of pure ZnO sample is about 1141 degrees Celsius, showing the ratio of fuel to sufficient oxidant resources (F/O=1.17). With aluminum nitrate increasing, this ratio also rises (F/O=2.06). This increase shows the reduction of fuel to oxidant resources. By doping the fuel, combustion intensity also decreases so that the combustion temperature in the ZnO : Ag·Al sample reaches its lowest content of 481.48 degrees Celsius.

5. Fourier Transform Infrared Spectra (FT-IR)

Considering the entrance of dopant to the ZnO sample (Fig. 5), we observed peak shifts; therefore, the range of peaks was determined. In any sample, 3,000 cm^{-1} to 3,440 cm^{-1} peaks were attributed to O-H bands. The presence of O-H peaks has an important role in modifying photocatalytical properties. OH groups in significant conditions produce an electron and a hole that transfers electrons and reacts with free radicals available in the dye [24,30]. The peaks in 2,300 cm^{-1} range show C-N bonds. The peaks in 2,900 cm^{-1} to 2,930 cm^{-1} range are attributed to C-H bonds. The peak corresponding to the bending vibration of water on the surface of the material is in the range of 1,640 cm^{-1}. Among the known ranges of peaks, the peak in 1,400 cm^{-1} is related to N-O bonds that are created of residual nitrate resources of combustion. This peak is sharper in the calcined sample, which shows the purity of the trapped compound in the structure. In all samples, peaks due to stretching

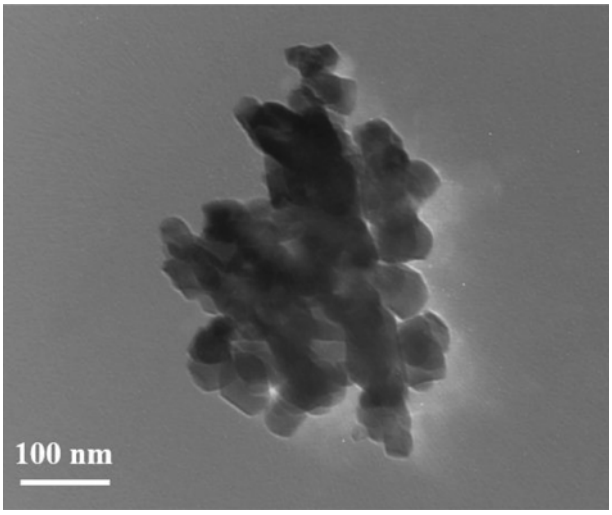

Fig. 3. TEM image of ZnO doped with 7% mol Ag and 15% mol Al.

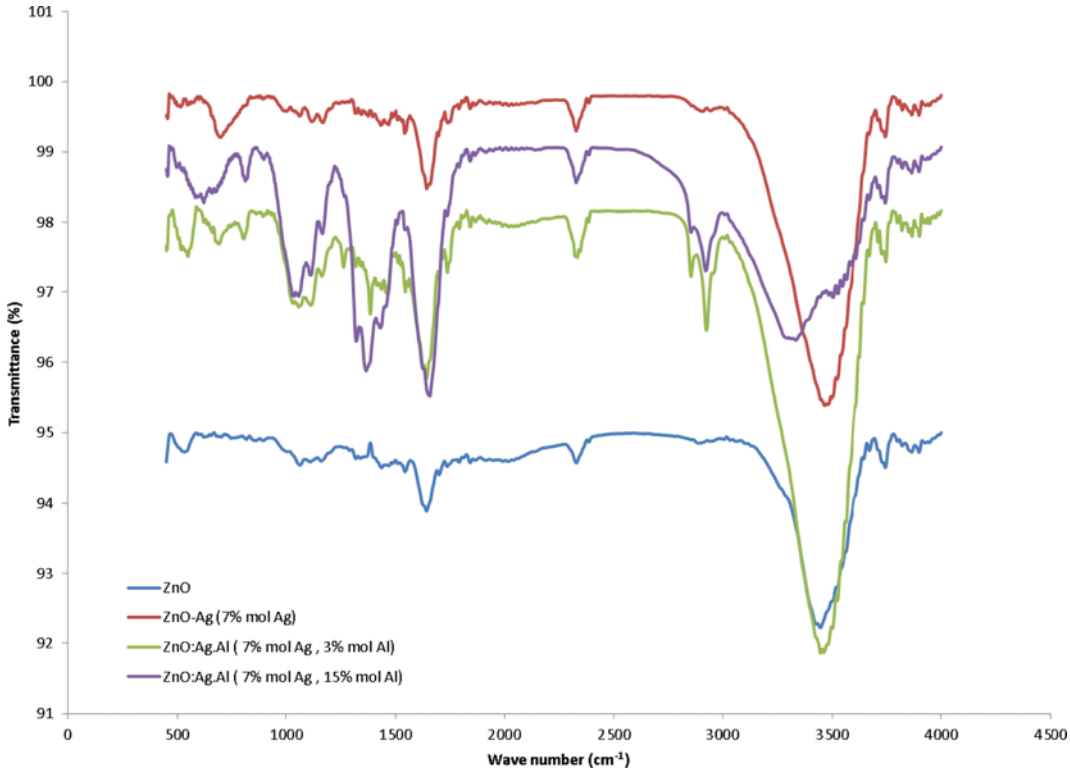

Fig. 5. FTIR of dopant to the ZnO sample.

vibrations of ZnO_4 are revealed in the range of 458 to 467 cm^{-1}. By adding aluminum nitrate to the samples the intensity of peaks related to weak bond of Al-O increases. These peaks can be observed in the range of 1,000 to 1,070 cm^{-1}. The peak observed at 1,200 cm^{-1} also shows the trapped carbon dioxide derived from combustion conditions and is the double stretching bond of C=O.

6. Absorption Edge and Band Gap

The absorption spectra of different samples are presented in

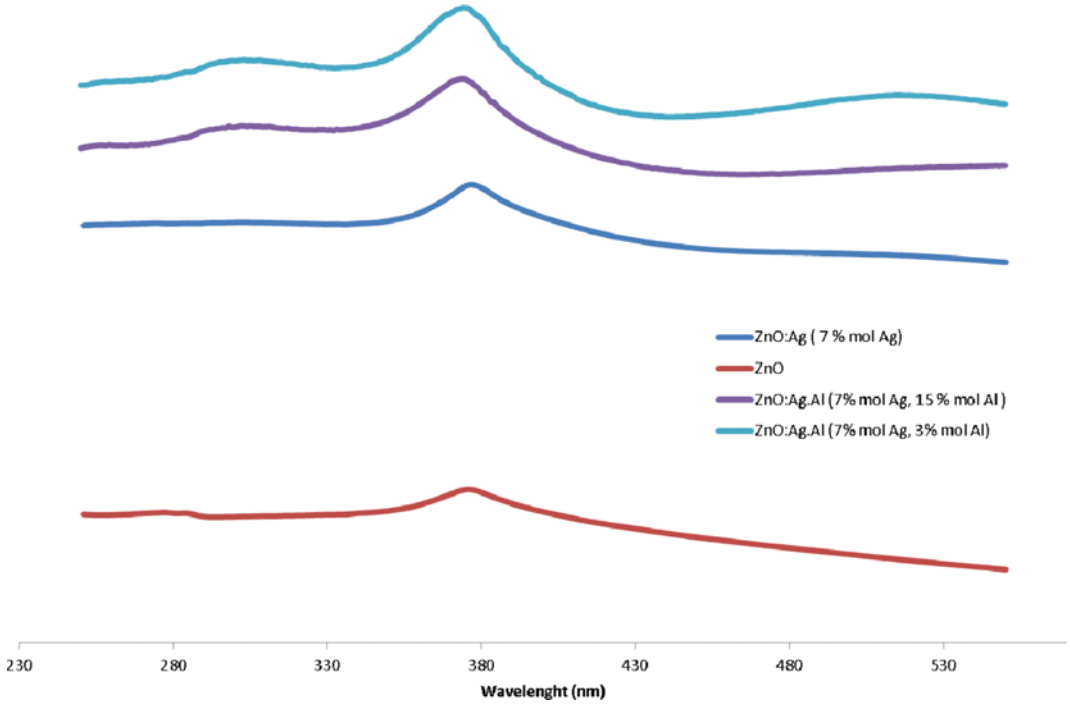

Fig. 6. Absorption spectra of ZnO and Al-Ag doped to ZnO sample.

Fig. 6. The absorption edges are located at 380 nm. It can be seen that the silver and aluminum addition does not make any significant change in absorption edge of ZnO. However, the approximate determination of band gap was calculated by Tauc's plot, in which $(\alpha h\nu)^{1/n}$ is plotted as a function of $h\nu$ (photon energy).

$$(\alpha h\nu)^{\frac{1}{n}} = A(h\nu - E_g) \quad (7)$$

where h is Planck's constant, α is the absorption coefficient, ν is the frequency of photon, A is the optical constant and n value is 2 for indirect transitions. The intersection between the linear fit and the photon energy axis gives the value to the band gap energy (E_g) [31].

In many nanoscale materials a dependence of the band gap is observed as a function of particle size - owing to the spatial confinement of the low energy band edge states to within the particle. Change in band gap calculated with Tauc Plots can be attributed to surface oxygen vacancies and defects, which can cause the more intense photocatalytic activity [32]. Surface defect contributions of Ag and Al on ZnO make it more complex for competitive recombination pathways and absorption edge value. The same value in absorption edge peak can be attributed to the tail region of the above UV emission due to recombination of electron and hole at band states of ZnO [33]. Then, if particle size distribution is thick, the value obtained from a distribution of gap energies may appear broadened due to an absorption spectrum.

As shown in Fig. 7, the determined band gap of ZnO : Ag·Al (7% mol Ag, 3 mol% Al) was 3.026 eV. However, as the doped Al molar ratio increased, the band gap (E_g) of catalyst powder increased from 3.022 eV to 3.17 eV for ZnO : Ag·Al (7% mol Ag, 15 mol% Al). Band gap depends on the fabrication technique, surface quality, size and diameter of ZnO [34]. However, incorporation of Al_2O_4 can induce an increase in band gap on the surface of ZnO. The band gap of other samples which were determined by mentioned technique is shown in Table 1.

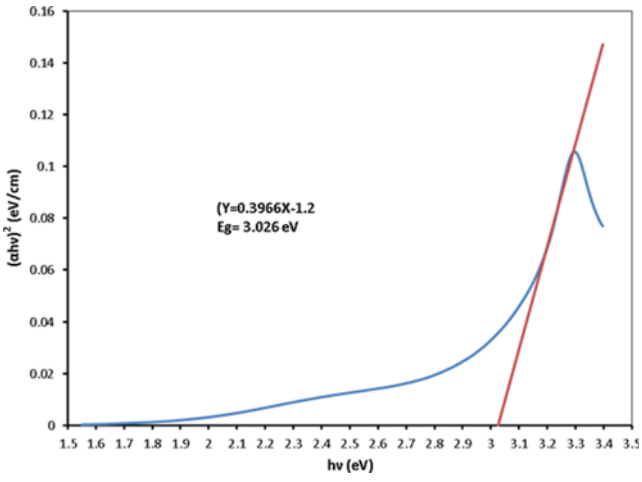

Fig. 7. Band gap energy of ZnO : Ag·Al (7% mol Ag, 3 mol% Al).

7. Effect of Ag and Al Amount on ZnO Photocatalytic Activity

Different molar ratios of Ag and Al have been examined to find the best amounts of Al and Ag as impurities for ZnO photo catalyst. A fixed optimum operating condition (pH=8, 0.1 $g \cdot L^{-1}$ photocatalyst dosage, 20 mg/L RB19 solution) and a batch reactor with low pressure mercury lamp (OSRAM, 15w) were employed to investigate the effect of species doped with ZnO. Before the UV irradiation, solution of the day and catalysts was circulated in reactor in order to achieve adsorption/desorption equilibrium. During certain times, 4 ml of solution was immediately centrifuged for decolorization process by ultraviolet-visible (UV-Vis) absorption double beam spectrophotometer. It was observed that less than 10 present of RB19 decolorized in absence of UV radiation. The decolorization percentage of organic compound can be calculated as follows:

$$\text{Decolorization efficiency} = \left(1 - \frac{A}{A_o}\right) \times 100 \quad (8)$$

where A and A_o are the dye concentration at time t and t=0, respectively.

Photocatalytic activity of ZnO can be increased by adding a small amount of silver. Color removing efficiency can be achieved to 80% at the 7 mol% of silver loading. The modified zinc oxide with an appropriate amount of silver can prevent recombination of electrons and holes in ZnO. Performance of zinc oxide can be significantly affected by reducing defects on the ZnO surface and chemical adsorption of oxygen molecules or oxygen atoms [35]. On the other hand, an increase in electron transfer to silver metallic can be attributed to the higher conduction band energy level of ZnO than Fermi energy level of Ag [36,37], which explains the increase in the efficiency of zinc oxide catalyst in the presence of silver. In addition, photocatalytic efficiency of ZnO : Ag nanocomposite increases with adding Al content. It has been observed that the optimum Al content for maximum catalytic activity is about 3 mol% (Fig. 8). Next, the color degradation gradually decreases with increasing Al content to reach 15 mol%. This may be attributed to the lower surface area of ZnO than incorporation of aluminum oxide clusters on the surface of zinc oxide, light adsorption of ZnO will be blocked by excessive aluminum. From the above, the following mechanism can be suggested: The enhancement of mesoporous Al_xO_y (x=1-2, y=1-5) - ZnO composite can be explained by the fact that ZnO is the more photoactive than aluminum oxide for photocatalysis reactions. The addition of aluminum at low content onto ZnO particles led to the better electrical properties effect (Scheme 1) and hence increased the separation efficiency of charge carriers [38].

8. Effect of pH

Because of the amphoteric behavior of semiconductor oxides,

Table 1. Absorption spectra of ZnO and Al-Ag doped to ZnO sample

Catalyst	ZnO	Ag/ZnO (7% mol Ag)	Al-Ag/ZnO (3% mol Al & 7% mol Ag)	Ag-Al/ZnO (15% mol Al & 7% mol Ag)
Band gap (eV)	3.03	3.022	3.026	3.17

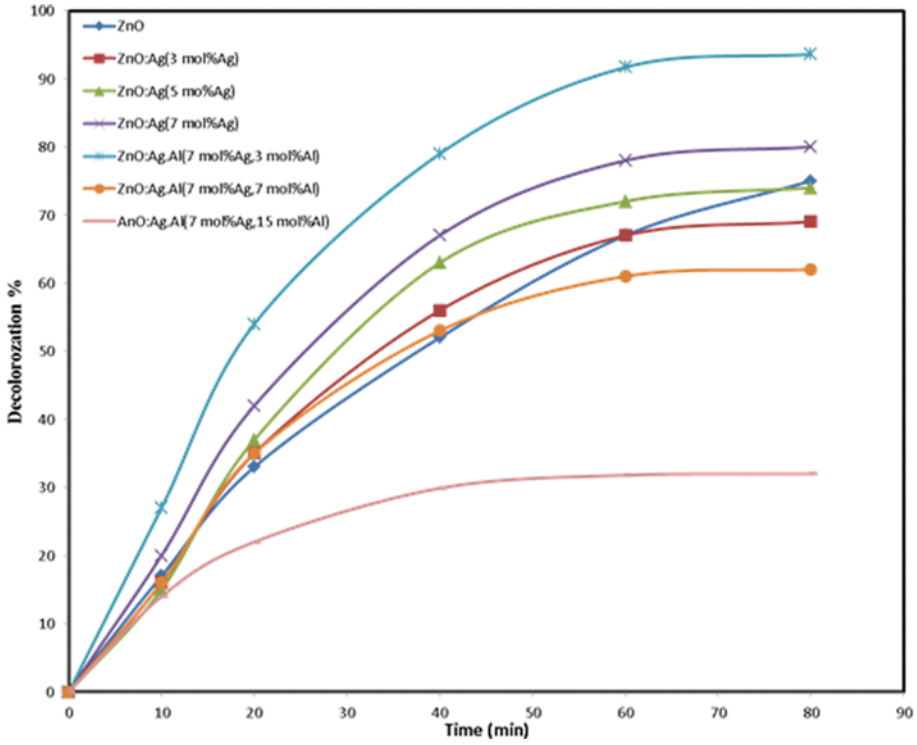

Fig. 8. Decolorization efficiency of ZnO with different amount of Doped materials versus time (RB19 concentration=20 ($mg{\cdot}L^{-1}$), pH=8, time=80 min).

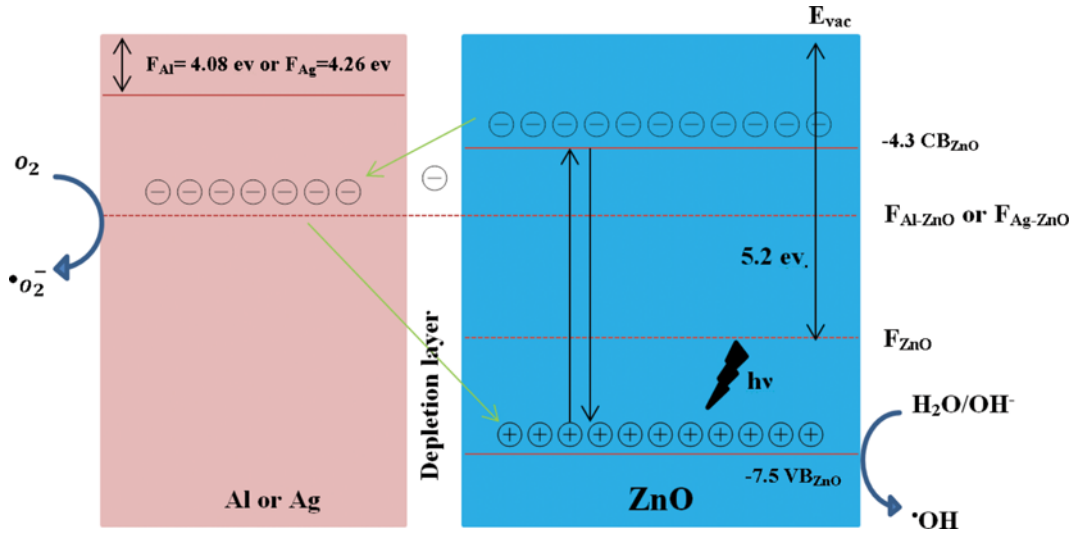

Scheme 1. Schematic illustration of proposed mechanism to explain the enhancement photonic efficiency into nanomaterials for photodegradation of RB19.

the effect of pH on the reaction rate was also studied in this work. Variation of pH affects the electron charge on surface of catalyst [39] and dye degradation process under UV light irradiation [40]. Decolorization of RB19 at different range of pH from 3 to 10 with a certain amount of optimum catalyst (0.1 gr/lit) was investigated. Dye removing efficiency was quite low at pH=3, but at pH within the 8 the average decolorization rate was about 85% during one hour.

Zinc oxide, which is an amphoteric oxide and can be hydrolyzed in water to produce hydroxide layers, reacts with H^+ or OH^- according to the following equations [4,41,42]:

$$\text{In acid: } ZnO+2H^+ \rightarrow Zn_2^+ + H_2O \quad (9)$$

$$\text{In base: } ZnO+H_2O+2\,OH^- \rightarrow [Zn(OH)_4]^{2-} \quad (10)$$

There are electrostatic forces between the catalyst and the color that are influenced by pH. So finding the pH at the zero charge (pH_{pzc}) is important. At the pH_{pzc}, catalyst surface charge is positive, while at higher pH values a negative charge on the surface due to

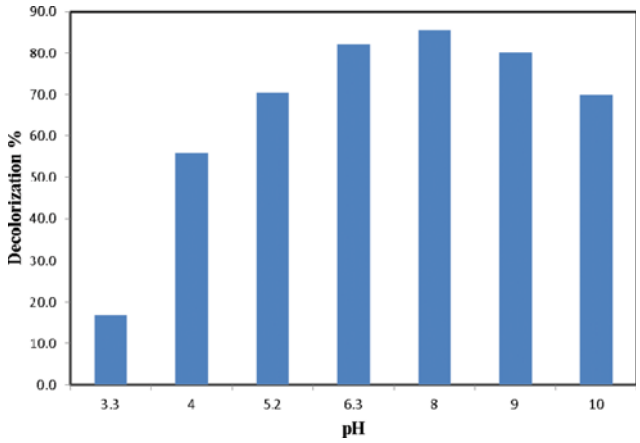

Fig. 9. Effect of pH on decolorization of RB19. Dye solution=20 (mg·L^{-1}), catalyst dosage (ZnO : Ag·Al)=0.1 g/L, 7% mol Ag & 3% mol Al.

the greater presence of $^{\bullet}OH$ is observed [43]. Thus, there is a strong affinity between RB19 and catalyst surface for 3<pH<10 that causes different photocatalytic effects. As shown in Fig. 9, the optimum pH range for high removal efficiency of dye is 8.

9. Recyclability and Mechanism of Catalyst

To study recyclability and stability of optimal catalyst, it was tested three times. In each run it was separated by centrifuge, washed three times with deionized water to remove any adsorbed organic compounds, and allowed in oven to dry. RB19 degradation efficiency using ZnO : Ag·Al dropped from 93% to 81% after three cycles, which was comparable to ZnO (Fig. 10). However, the surface poisoning, which is induced by adsorbed intermediates, may be one reason for deactivation of photocatalyst after each run [44]. Also, in case of ZnO, 65% of degradation efficiency was obtained for RB19 after three times.

ZnO, Ag and Al have a work function of 5.2 and 4.26 eV and 4.08 eV, respectively [34]. The Fermi energy level of Ag (F_{Ag}) and Al (F_{Al}) was higher than that of ZnO (F_{ZnO}) because of the larger work function of ZnO. This leads to the transfer of electrons from Fermi level of Ag (F_{Ag}) or Al (F_{Al}) to Fermi level of ZnO (F_{ZnO}), until the two levels attain equilibrium and form the new Fermi energy level ($F_{ZnO:Ag\cdot Al}$) [45].

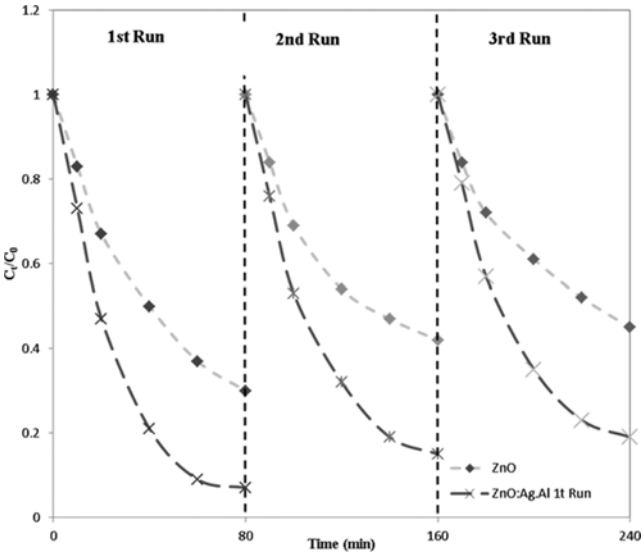

Fig. 10. Cycling photodegradation curves of RB19 over ZnO and ZnO : Ag·Al (7% mol Ag & 3% mol Al).

Upon UV irradiation, electrons are excited from the valence band of ZnO to its conduction band, leaving the corresponding holes in the valence band. Since the conduction band of ZnO is higher in energy than the new equilibrium Fermi energy level ($F_{ZnO:Ag\cdot Al}$) of ZnO : Ag·Al, the photoexcited electrons on the conduction band are transferred from ZnO to Ag and Al [46]. Thus the separation efficiency of the photogenerated electrons and holes is enhanced. The photogenerated holes in the valence band of ZnO react with water and hydroxyl groups to form hydroxyl radicals, which leads to the photocatalytic oxidation of the dye. At the same time, the photogenerated electrons react with O_2 to form active oxygen species, which also participate in the photocatalytic oxidation of the dye. This process can be expressed as follows:

$$ZnO:Ag\cdot Al + h\nu \rightarrow ZnO:Ag\cdot Al\ (h^+ + e^-) \quad (11)$$

$$h^+ + H_2O \rightarrow {}^{\bullet}OH + H^+ \quad (12)$$

$$e^- + O_2 \rightarrow {}^{\bullet}O_2^- \quad (13)$$

$${}^{\bullet}O_2^- + H_2O \rightarrow H_2O_2 \rightarrow 2{}^{\bullet}OH \quad (14)$$

$$RB19 + {}^{\bullet}O_2^- \text{ or } {}^{\bullet}OH \rightarrow \text{the decomposed products} \rightarrow CO_2 + H_2O \quad (15)$$

CONCLUSION

Microwave-assisted combustion synthesis (MACS) was used to fabricate Al doped ZnO : Ag. According to Scherrer's equation and TEM test, ZnO : Ag·Al photocatalyst has a crystallite size of 40 to 50 nm. However, the conditions of combustion synthesis and ratio of fuel to oxidants may influence the particle size. SEM test showed that by increasing aluminum nitrate content in the samples, the plate formation varies to have a less porosity, which is discussable with thermodynamic analysis. There was no respectable change in absorption edge and band gap of ZnO : Ag·Al nanomaterial in comparison with pure ZnO. The catalytic activities of samples were investigated by degradation of Reactive Blue 19 under UV radiation in a batch reactor. This experiment showed ZnO : Ag·Al (7 mole% Ag and 3% mole Al) has more catalytic property to degrade dye pollution than ZnO. Also, it illustrated that a distinct amount of Al can enhance the catalyst activity, and more than 3% molar aluminum can slightly decrease the catalytic activity and increase the adsorption behavior of the particle. Studies revealed that pH=8 is an optimum condition for decolorization of 20 mg/*l* RB19 solution with 0.1 g/L catalyst dosage. Optimum synthesized catalyst showed good stability under three times recycling, and its efficiency for degradation of RB19 dropped from 93% to 81% after three cycles compared with ZnO.

REFERENCES

1. C. Karunakaran, V. Rajeswari and P. Gomathisankar, *Superlattices*

and Microstructures, **50**, 234 (2011).
2. M. Ahmad, E. Ahmedb, Y. Zhang, N. R. Khalid, J. Xu, M. Ullah and Z. Hong, *Curr. Appl. Phys.*, **13**, 697 (2013).
3. R. K. Sharma, S. Patel and K. C. Pargaien, *Adv. Nat. Sci: Nanosci. Nanotechnol*, **3**, 035005 (2012).
4. C. H. Wu, *Hazard. Mater.*, **153**, 1254 (2008).
5. C. Karunakaran, V. Rajeswari and P. Gomathisankar, *Solid State Sciences*, **13**, 923 (2011).
6. E. Burunkaya, N. Kiraz, O. Kesmez, H. E. Camurlu, M. Asilturk and E. Arpac, *Sol-Gel Sci. Technol.*, **55**, 171 (2010).
7. S. Mondal, S. R. Bhattacharyya and P. Mitra, *Physics*, **80**, 315 (2013).
8. L. Wang, Q. Hu, Z. Li, J. Guo and Y. Li, *Mater. Lett.*, **79**, 277 (2012).
9. J. Iqbal, T. Jan, M. Ismail, N. Ahmad, A. Arif, M. Khan, M. Adil and A. Arshad, *Ceramics International in Press*, **40**, 7487 (2013).
10. G. Lia, X. Zhua, X. Tanga, W. Songa, Z. Yanga, J. Daia, Y. Suna, X. Panb and S. Daib, *Alloys Compounds*, **509**, 4816 (2011).
11. S. Ameen, M. Shaheer Akhtar, H. K. Seo, Soon Kim, Y., Shik Shin, H., *Chem. Eng.*, **187**, 351 (2012).
12. W. Xie, Y. Li, W. Sun, J. Huang, H. Xie and X. Zhao, *Photochemistry and Photobiology A: Chemistry*, **216**, 149 (2010).
13. C. Aydın, M. S. Abd El-sadek, K. Zheng, I. S. Yahia and F. Yakuphanoglu, *Optics Laser Technol.*, **48**, 447 (2013).
14. H. J. Son, K. A. Jeon, C. E. Kim, J. H. Kim, K. H. Yoo and S. Y. Lee, *Optics Laser Technol.*, **48**, 447 (2013).
15. Q. Simon, D. Barreca, D. Bekermann, A. Gasparotto, C. Maccato, Elisabetta, V. Gombac, P. Fornasiero, O. I. Lebedev, S. Turner, A. Devi, R. A. Fischer and G. V. Tendeloo, *Hydrogen Energy*, **36**, 15527 (2011).
16. S. Mitra, K. Sridharan, J. Unnam and K. Ghosh, *Thin Solid Films*, **516**, 798 (2008).
17. A. A. Ismail, A. El-Midany, E. A. Abdel-Aal and H. El-Shall, *Mater. Lett.*, **59**, 924 (2005).
18. L. C. Nehru, V. Swaminathan and C. Sanjeeviraja, *Powder Technol.*, **226**, 29 (2012).
19. Barin, Juliano S., Flores, Érico M. M., Mesko, Márcia F., Mello, Paola A., Pereira, Juliana S. F., Chapter 5 - Microwave-Induced Combustion. *Microwave-Assisted Sample Preparation for Trace Element Analysis*, 143 (2014).
20. B. Subash, B. Krishnakumar, M. Swaminathan and M. Shanthi, *Mater. Sci. Semiconductor Processing*, **16**, 1070 (2013).
21. I. Khan, S. Khan, R. Nongjai, H. Ahmed and W. Khan, *Optical Mater.*, **35**, 1189 (2013).
22. A. Jagannatha Reddya, M. K. Kokilab, H. Nagabhushanac, J. L. Raod, B. M. Nagabhushanae, C. Shivakumaraf and R. P. S. Chakradharg, *Spectrochim. Acta Part A: Molecular and Biomolecular Spectroscopy*, **79**, 476 (2011).
23. Y. T. Prabhu, K. V. Rao and V. S. S. K. Kumar, *Adv. Nano.*, **2**, 45 (2013).
24. J. Sivasankari, S. Sankar, S. Selvakumar, L. Vimaladevi and R. Krithiga Synthesis, *Mater. Chem. Phys.*, **143**, 1528 (2013).
25. S. Rasouli and S. Jebeli Moeen, *Alloys Compounds*, **509**, 1915 (2011).
26. S. Ekambarama, Y. Iikubo and A. Kudo, *Alloys Compounds*, **433**, 237 (2007).
27. R. Ianos, I. Lazaua, C. Pacurariua and P. Sfîrloagab, *Mater. Chem. Phys.*, **129**, 881 (2011).
28. C.-C. Hwang and T.-Y. Wu, *Mater. Sci. Eng. B*, **111**, 197 (2004).
29. S. K. Sharma, S. S. Pitale, M. Manzar Malik, R. N. Dubey, M. S. Qureshi and S. Ojha, *Phys. B: Condensed Matter*, **405**, 866 (2010).
30. N. L. Tarwal, P. R. Jadhav, S. A. Vanalakar, S. S. Kalagi, R. C. Pawar, J. S. Shaikh, S. S. Mali, D. S. Dalavi, P. S. Shinde and P. S. Patil, *Powder Technol.*, **208**, 185 (2011).
31. R. P. Antony, T. Mathews, P. K. Ajikumar, D. N. Krishna, S. Dash and A. K. Tyagi, *Mater. Res. Bulletin*, **47**, 4491 (2012).
32. B. Chain, X. Wang, S. Cheng, H. Zhou and F. Zhang, *Ceramics International*, **40**, 429 (2014).
33. B. Pal, S. Dhara, P. K. Giri and D. Sarkar, *Alloys Compounds*, **615**, 378 (2014).
34. K. F. Lin, H. M. Cheng, H. C. Hsu, L. J. Lin and W. F. Hsieh, *Chem. Phys. Lett.*, **409**, 208 (2005).
35. R. Mohan, K. Krishnamoorthy and S.-J. Kim, *Chem. Phys. Lett.*, **539-540**, 83 (2012).
36. B. Divband, M. Khatamian, G. R. Kazemi Eslamian and M. Darbandi, *Appl. Surf. Sci.*, **284**, 80 (2013).
37. A. Aprilia, P. Wulandari, V. Suendo, Herman, R. Hidayat, A. Fujii and M. Ozaki, *Sol. Energy Mater. Sol. Cells*, **111**, 181 (2013).
38. D. R. Sahu, S. Y. Lin and J. L. Huang, *Solar Energy Mater. Solar Cells*, **91**, 851 (2007).
39. M. Shahla N. and S. M. Tabatabaei, *Young Researchers and Elite Club*, **2** (2000).
40. G. A. Gomez, M. B. Veldman, Y. Zhao, S. Burgess and S. Lin, *PLoS ONE.*, **4**(3) (2009).
41. Li PUMA, G., *Chem. Eng. Res. Design*, **83**, 820 (2005).
42. C. E. Housecroft and A. G. Sharpe, Inorganic Chemistry (2nd Ed.). *Prentice Hall*. P.173 ISBN 978-0130399137 (2004).
43. M. Ba-Abbad, A. A. H. Kadhum, A. B. Mohamad, M. S. Takriff and K. Sopian, *J. Alloys Compd.*, **550**, 63 (2013).
44. O. S. Ayanda, O. S. Fatoki, F. A. Adekola and B. J. Ximbaa, *Marine Pollution Bulletin*, **72**, 222 (2013).
45. R. Saravanan, N. Karthikeyan, V. K. Gupta, E. Thirumal, P. Thangadurai, V. Narayanan and A. Stephen, *Mater. Sci. Eng.*, **4**, 2235 (2013).
46. S. Pyne, G. P. Sahoo, D. K. Bhui., H. Bar, P. Sarkar, S. Samanta, A. Maity and A. Misra, *Spectrochim. Acta Part A: Molecular and Biomolecular Spectroscopy*, **93**, 100 (2012).